ELSEVIER

Journal of Fluids and Structures 23 (2007) 1106–1118

JOURNAL OF FLUIDS AND STRUCTURES

www.elsevier.com/locate/jfs

Jet impingement on cylindrical cavity: Conical nozzle considerations

S.Z. Shuja, B.S. Yilbas*, M.O. Budair

ME Department, KFUPM, Dhahran 31261, Saudi Arabia

Received 20 September 2005; accepted 24 March 2007
Available online 8 August 2007

Abstract

In laser gas-assisted processing, the assisting gas emerges from a nozzle and nozzle geometric configurations alter the flow structure and heat transfer characteristics in and around the section processed. In the present study, the influence of nozzle geometric configurations, cavity diameter and depth, on flow structure and heat transfer rates from the cavity is investigated. A cylindrical cavity with two diameters and varying depths is accommodated in the simulations. Air is used as assisting gas while steel is employed as workpiece material. A numerical scheme using a control volume approach is accommodated to discretize the flow and energy equations. It is found that flow structure changes significantly for large diameter cavity. The influence of the nozzle cone angle on heat transfer and flow structure is more pronounced as the cavity depth increases.

Keywords: Conical nozzle; Jet impingement; Cavity

1. Introduction

Nozzles are one of the important elements in laser gas-assisted processing. Conical nozzles are widely used to discharge the assisting gas impinging onto a workpiece surface during laser processing of solid substrates. Depending on the nozzle geometric configuration, mainly the nozzle cone angle, the flow structure around the laser irradiated region may be modified. This in turn results in changing of heat transfer rates from the irradiated region and drag forces along the surfaces. However, during the laser processing, in the initial state, a cavity is formed, which may be considered as a cylindrical cavity, particularly during the drilling process. Consequently, investigation into flow structure and heat transfer characteristics due to the geometric configuration of the nozzle geometry and hole size becomes necessary.

Considerable research studies were carried out to investigate the laser gas-assisted processing. The scaling law was proposed by Kar et al. (1992) for laser gas-assisted processing. They indicated that the model predictions agreed well with the experimental results. The dynamic characteristics of gas flow inside a laser-generated cut kerf were studied by Man et al. (1997). They computed the conical nozzles with supersonic nozzles and indicated that the nozzle exit-to-workpiece spacing had considerable influence on the flow structure for a supersonic nozzle. The influence of the assisting gas pressure on the laser cutting process was examined by Chen (1998). He showed that clear edge cutting could result for certain combinations of cutting parameters. Off-axial gas-assisted cutting of a thick steel workpiece was

*Corresponding author. Tel.: +966 3 8604481; fax: +966 3 8602949.
E-mail address: bsyilbas@kfupm.edu.sa (B.S. Yilbas).

0889-9746/$ - see front matter
doi:10.1016/j.jfluidstructs.2007.03.005

studied by Hsu and Molian (1995). They showed that the dual gas jet cutting is very effective for laser cutting of thick samples. Yilbas et al. (1995) studied the influence of assisting gas on laser cutting process. They showed that the chemical reaction contribution to energy content in the cutting section was about 60%.

Since the gas jet emerging from the nozzle impinges onto an irradiated workpiece surface, the jet impingement studies are important in laser gas-assisted processing. Considerable research studies were carried out to examine the gas jet impingement onto surfaces. The heat transfer rates from flat surfaces due to jet impingement were investigated by Huang and El-Genk (1994). They indicated that the Nusselt number was maximized for certain nozzle exit-to-plate spacing. The measurement of the heat transfer coefficient due to jet impingement onto flat surfaces was carried out by Bizzak and Chyu (1995). They indicated that the measurement results agreed well with the previously obtained data. Mohanty and Tawfek (1993) studied heat transfer rates from flat surfaces due to round jet impingement. They defined the active area of nozzle and measured the heat transfer rates from the surface. The confined and submerged liquid jet impingement heat transfer rates were studied by Garimella and Rice (1995). They indicated that secondary peaks in the local heat transfer were observed at a ratio of $r/d \approx 2$ (radial distance from stagnation point to nozzle diameter). This was more pronounced at small spacings and large nozzle diameters for a given Reynolds number. Yilbas et al. (2002) investigated jet impingement onto flat surfaces and the influence of jet velocity profiles on heat transfer characteristics. They showed that a velocity power law of $\frac{1}{10}$ power gave results in agreement with the previously obtained data. Yilbas et al. (2003) studied jet impingement onto a parallel sided hole. They indicated that the mass flow rate passing through the hole was influenced considerably by the depth of the hole. Yilbas et al. (2004) investigated flow into a conical cavity. They showed that the stagnation region moved into the cavity entry as the cavity depth increased.

In the present study, gas jet emerging from a conical nozzle and impinging onto a cylindrical cavity is considered. The influence of nozzle cone angle, cavity diameter, and cavity depth on flow structure and heat transfer characteristics around the cavity is investigated. A numerical scheme employing a control volume approach is introduced to discretize the governing flow and energy equations.

2. Mathematical modelling

In laser gas-assisted processing, the impinging jet conditions are mainly steady; consequently, steady flow conditions are considered in the analysis, provided that the compressibility effect and variable properties are accommodated. The jet impinging onto a cylindrical cavity is simulated. The heat source with a constant heat flux is considered at the plate surface. A three-dimensional view and the geometric arrangements of the conical nozzle and the cavity are shown in Fig. 1, while the nozzle and the cavity configurations are given in Tables 1 and 2, respectively.

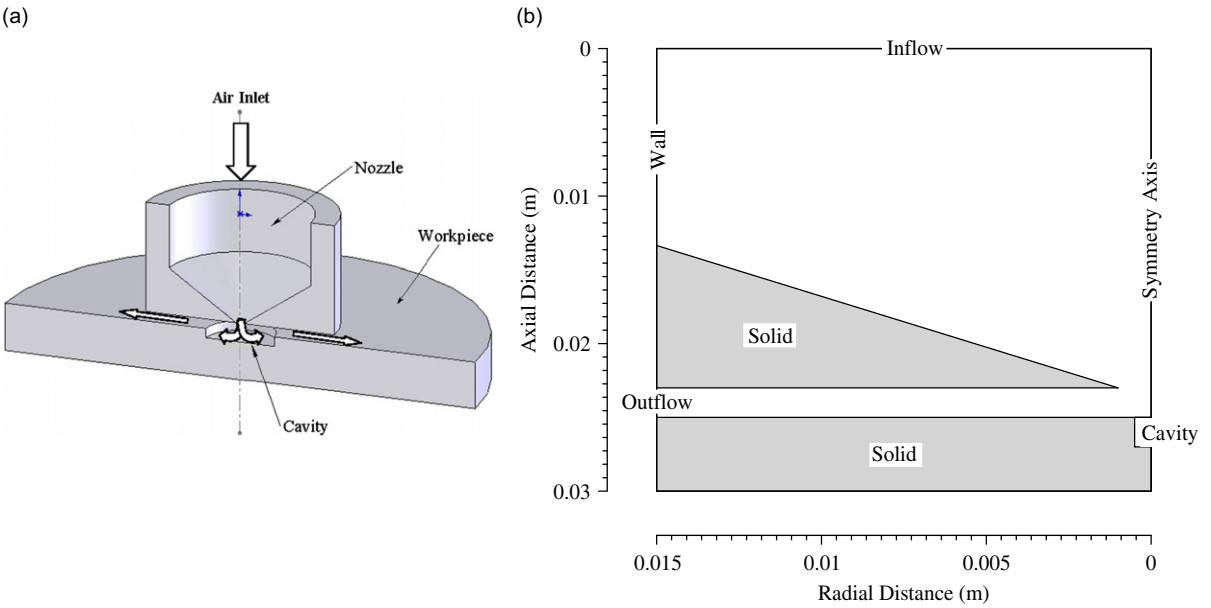

Fig. 1. (a) 3-dimensional view of nozzle and workpiece assembly, and flow directions; (b) lay out of the solution domain.

Table 1
Geometry configuration of conical nozzle

Nozzle #	Cone angle, θ (deg)
1	55
2	60
3	65
4	70

Table 2
Depth and size of the cavities

Cavity diameter (m)	Cavity depth (m)
0.001	0.0000
0.003	0.0002
	0.0005
	0.001
	0.002

2.1. Flow equations

The governing flow and energy equations for the axisymmetric impinging jet can be written in the Cartesian tensor notation as

(i) the continuity equation:

$$\frac{\partial}{\partial x_i}(\rho U_i) = 0; \tag{1}$$

(ii) the momentum equation:

$$\frac{\partial}{\partial x_i}(\rho U_i U_j) = -\frac{\partial p}{\partial x_j} + \frac{\partial}{\partial x_i}\left[\mu\left(\frac{\partial U_i}{\partial x_j} + \frac{\partial U_j}{\partial x_i}\right) - \rho R_{ij}\right]; \tag{2}$$

(iii) the energy equation:

$$\frac{\partial}{\partial x_i}(\rho U_i H) = \frac{\partial}{\partial x_i}\left[\frac{\mu}{\sigma}\frac{\partial H}{\partial x_i} - \rho R_{ih}\right]. \tag{3}$$

When modelling the Reynolds stresses and turbulence properties the following steps are considered. The Reynolds stress turbulence model (RSTM) is based on the second-moment closure (Launder, 1989). The transport equation of the Reynolds stress (R_{ij}) is

$$\frac{\partial}{\partial x_m}(U_m R_{ij}) = P_{ij} + \Lambda_{ij} - \varepsilon_{ij} + \Pi_{ij} + \Pi^w_{ij}, \tag{4}$$

where P, Λ, ε, Π and Π^w are the rate of production, transport by diffusion, rate of dissipation, transport due to turbulent pressure excluding strain interactions and transport due to wall reflection, respectively. Eq. (4) consists of six partial differential equations; one for the transport of each of the six independent Reynolds stresses. The production term (P_{ij}), diffusion (Λ_{ij}), dissipation (ε_{ij}), transport due to turbulent pressure (Π_{ij}) and the modelling of the wall reflection (Π^w_{ij}) are referred to Launder (1989).

2.2. Flow boundary conditions

Four boundary conditions are considered in accordance with the geometric arrangement of the problem, as shown in Fig. 1.

2.2.1. Solid wall

For the solid wall, the no-slip condition is assumed at the solid wall, and the boundary condition for the velocity at the solid wall therefore is

$$U_i = 0. \tag{5}$$

2.2.2. Generalized wall functions for normal and shear turbulent stresses for the RSTM model

When the flow is very near the wall, it undergoes a rapid change in direction, the wall-functions approach is not successful in reproducing the details of the flow. Consequently the turbulent stresses and fluxes at the near-wall grid points are calculated directly from their transport equations. In this case, the near-wall region lying between the wall and the near-wall computational node at x_p can be represented by two layers: the fully viscous sublayer, defined by $\mathrm{Re}_v = x_v\sqrt{k_v}/\nu \simeq 20$, and a fully turbulent layer. The wall shear stress near the wall is employed, i.e. $\overline{vw}|_{z_v} = \tau_w/\rho$, which serves as the boundary condition for the $\overline{vw}$ transport equation.

In relation to normal stresses, the turbulence energy must decrease quadratically towards a value of zero at the wall (Benocci, 1991), therefore a zero-gradient condition for the normal stresses is physically realistic. This situation is insufficient to ensure an accurate numerical representation of near-wall effects. An improved approach for internal cells is needed in respect of evaluating volume-integrated production and dissipation of normal stresses (these are normally evaluated at cell centres, using linear interpolation, and then multiplied by the cell volume). Considering $\overline{v^2}$ as an example, the volume-integrated production of $\overline{v^2}$ between the wall and the P-node may be approximated by (Hogg and Leschziner, 1989), i.e.

$$\int_{\Delta r}\int_0^{z_p} P_{22}\,\mathrm{d}\forall \cong \int_{\Delta r}\int_{x_v}^{x_p} -2\overline{vw}\frac{\partial V}{\partial x}\,\mathrm{d}\forall = 2\tau_w\left(\frac{V_p - V_v}{x_p - x_v}\right)x_p\Delta r, \tag{6}$$

where V_p and V_v follow from the log-law. No contribution arises from the viscous sublayer, since $\overline{vw} = 0$ in this layer. An analogous integration of the dissipation rate with the assumptions,

$$\varepsilon = \frac{2\nu k_v}{x_v^2}, \quad 0 \leqslant x \leqslant x_v,$$

$$\varepsilon = \frac{C_\mu^{3/4}k_p^{3/2}}{\kappa x_v}, \quad x_v \leqslant x < x_p$$

leads to

$$\int_{\Delta r}\int_0^{x_p} \varepsilon\,\mathrm{d}\forall \cong \left[\frac{2\nu k_p}{x_v} + \frac{C_\mu^{3/4}k_p^{3/2}}{\kappa}\ln\left(\frac{x_p}{x_v}\right)\right]\Delta r; \tag{7}$$

an analogous treatment is applied to $\overline{v^2}$, while the production of $\overline{w^2}$ in the viscous and turbulent near-wall layers region is zero (Versteeg and Malalasekera, 1995).

The values resulting from Eqs. (6) and (7) are added, respectively, to the volume-integrated generation and dissipation computed for the upper half of the near-wall volume.

It should be noted that for the wall-law approach, the near-wall dissipation (ε_p) is not determined from its differential equation applied to the near-wall cell surrounding the node. Instead, and in accordance with the log-law, this value is obtained via the length scale from $\varepsilon_p = C_\mu^{3/4}k_p^{3/2}/\kappa z_p$, which serves as the boundary conditions for inner cells.

2.2.3. Inlet conditions

The boundary conditions for temperature and mass flow rate is introduced at nozzle inlet: T = specified (300 K) and $\dot{m}$ = specified (0.000225 kg s^{-1}).

The mass flow rate of the conical nozzles corresponding to the different configurations and for the pipe is kept the same. It should be noted that the pipe length is extended to secure the fully developed turbulent flow in the pipe before emerging from the pipe exit and impinging on to the cavity.

The values of k and ε are not known at the inlet, but can be determined from the turbulent kinetic energy, i.e.

$$k = \lambda \overline{u}^2, \tag{8}$$

where $\overline{u}$ is the average inlet velocity and λ is a percentage.

The dissipation is calculated from $\varepsilon = C_\mu k^{3/2}/aD$, where D is the diameter. The values $\lambda = 0.03$ and $a = 0.005$ are commonly used and may vary slightly in the literature (Elkaim et al., 1992).

2.2.4. Outlet

The flow is considered to be extended over a long domain; therefore, the boundary condition (outflow boundaries, Fig. 1) for any variable ϕ is

$$\frac{\partial \phi}{\partial x_i} = 0, \tag{9}$$

where x_i is the normal direction at outlet.

2.2.5. Symmetry axis

At the symmetry axis, the radial derivative of the variables is set to zero, i.e.

$$\frac{\partial \phi}{\partial r} = 0 \tag{10}$$

except for

$$V = \overline{vw} = \overline{vh} = \overline{wh} = 0. \tag{11}$$

2.3. Solid side

2.3.1. Constant wall temperature boundary

Two constant temperature boundaries are considered. The first one is in the radial direction far away from the symmetry axis at a constant temperature $T = T_{\text{amb}}$ (300 K) (boundary A in Fig. 1). It should be noted that the constant temperature boundary condition is set at different locations in the radial directions at boundary A and no significant effect of $T =$ constant was observed on the temperature and flow field in the stagnation region. Therefore, this boundary condition is set for a radial distance of 0.015 m from the symmetry axis. The second constant temperature boundary is set at the cavity walls (as shown in Fig. 1) at $T =$ constant (1500 K). A uniform heat flux boundary is considered at the cavity surface. The magnitude of the heat flux is set $1\,\mathrm{W\,m^{-2}}$.

2.3.2. Solid–fluid interface

The coupling of conduction within the solid and convection within the fluid, termed conjugation, is required for the present analysis at the solid fluid interface. The appropriate boundary conditions are continuity of heat flux and temperature and are termed boundary conditions of the fourth kind, i.e.

$$T_{w_{\text{solid}}} = T_{w_{\text{gas}}} \quad \text{and} \quad K_{w_{\text{solid}}} \frac{\partial T_{w_{\text{solid}}}}{\partial x} = K_{w_{\text{gas}}} \frac{\partial T_{w_{\text{gas}}}}{\partial x}. \tag{12}$$

No radiation losses from the solid surface is assumed.

2.4. Gas properties

The equation of state is used for air and the properties employed are given in Table 3.

Table 3
Air properties used in the simulation

Density, ρ ($\mathrm{kg\,m^{-3}}$)	p/RT
Thermal conductivity, K ($\mathrm{W\,m^{-1}\,K^{-1}}$)	0.0242
Specific heat capacity, c_p ($\mathrm{J\,kg^{-1}\,K^{-1}}$)	1006.43
Viscosity, v ($\mathrm{kg\,m^{-1}\,s^{-1}}$)	1.7894×10^{-5}

3. Numerical method and simulation

A control volume approach is employed when discretizing the governing equations. The discretization procedure is given in Patankar (1980). The problem of determining the pressure and satisfying continuity may be overcome by adjusting the pressure field so as to satisfy continuity. A staggered grid arrangement is used in which the velocities are stored at a location mid-way between the grid points, i.e. on the control volume faces. All other variables including pressure are calculated at the grid points. This arrangement gives a convenient way of handling the pressure linkages through the continuity equation and is known as Semi-Implicit Method for Pressure-Linked Equations (SIMPLE) algorithm. The details of this algorithm are given in Patankar (1980).

The computer program used for the present simulation can handle a nonuniform grid spacing. In each direction fine grid spacing near the gas jet impinging point and the cavity is allocated while gradually increased spacing for locations away from the cavity is considered. Elsewhere the grid spacing is adjusted to maintain a constant ratio of any of two adjacent spacings. The grid generated in the present study is shown in Fig. 2. The number of grid planes used normal to the x and r directions are 220 and 272, respectively, for the pipe and the conical nozzle. The grid independence tests were conducted and it is observed that the grid selected results in the grid-independent solution.

Nine variables are computed at all grid points; these are: two velocity components, local pressure, five turbulence quantities, and the temperature.

4. Results and discussions

The air jet emerging from a conical nozzle and impinging onto a conical cavity with different depths and diameters is considered. The influence of cone angle, cavity depth, and cavity diameter on the flow structure and heat transfer rates from the cavity side is examined.

Fig. 3 shows contours of velocity magnitude for four nozzle cone angles, two cavity diameters. The flow structures corresponding to two different cavity diameters differ significantly. In this case, impinging gas penetrates into the cavity, resulting in the stagnation zone moving inside the cavity for large diameters. However, jet penetration into the cavity is minimal for small diameter cavities, i.e. radial flow and streamline curving of the jet dominate almost over the edge of the cavity. Moreover, the streamline curving is not observed in the region above the cavity edges for the large cavity. Increasing the cone angle of the cavity modifies the flow structure in and around the cavity. This is particularly true for a large diameter cavity. The region of high-velocity magnitude along the symmetry axis reduces in size as the nozzle cone angle increases. This, in turn, results in a small circulation cell in the region close to the cavity sides, i.e. the

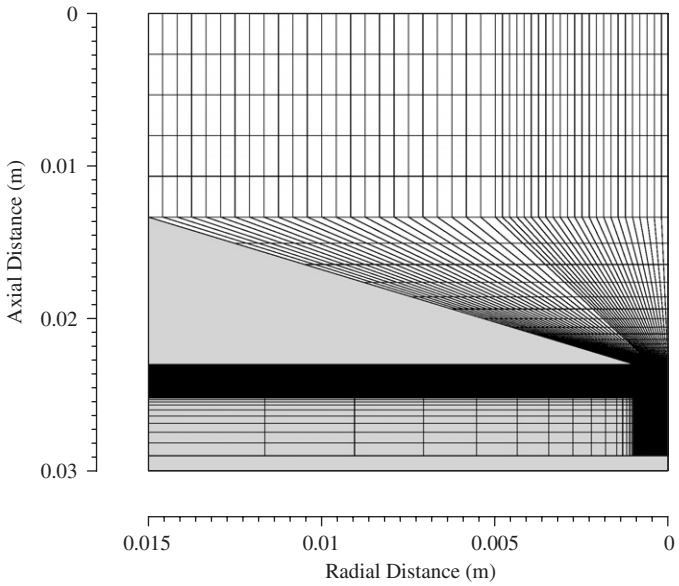

Fig. 2. Grid used in the numerical simulations.

reverse flow in the cavity results in a circulation cell. In the case of small diameter, no circulation cell is observed and the flow in the cavity is almost creeping-like flow.

Fig. 4 shows the velocity magnitude along the symmetry axis for two different cavity diameters, four nozzle cone angles, and five cavity depths. The jet emerging from a pipe is also shown for comparison. The expansion of the jet emerging from the nozzle is evident. Moreover, a cone angle of 40° results in the highest velocity magnitude downstream of the nozzle. Furthermore, the influence of cavity depth on the nozzle expansion is minimal for the small diameter cavity. In the case of the large diameter cavity, increasing cavity depth modifies the location of maximum velocity magnitude. The stagnation zone moves slightly the cavity for the small cavity diameter; however, it moves significantly inside into the cavity for the large cavity diameter. In the case of a jet emerging from a pipe, the velocity magnitude behaves similarly to that corresponding to a small diameter cavity. Moreover, this differs as the cavity depth increases.

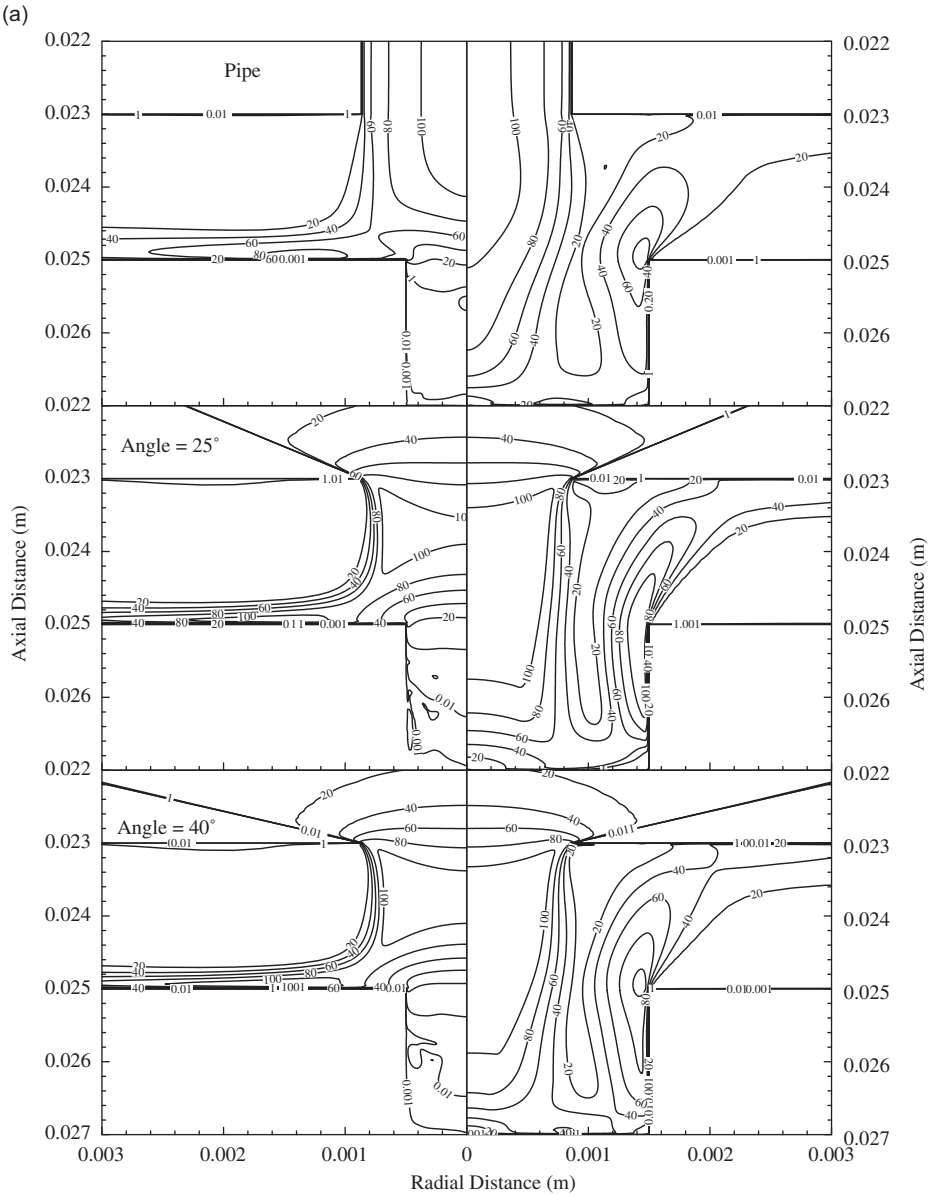

Fig. 3. Velocity magnitude contours for two cavity diameters: (a) two nozzle cone angles and pipe, and cavity depth 0.002 m; (b) nozzle cone angle of 25°, and different cavity depths.

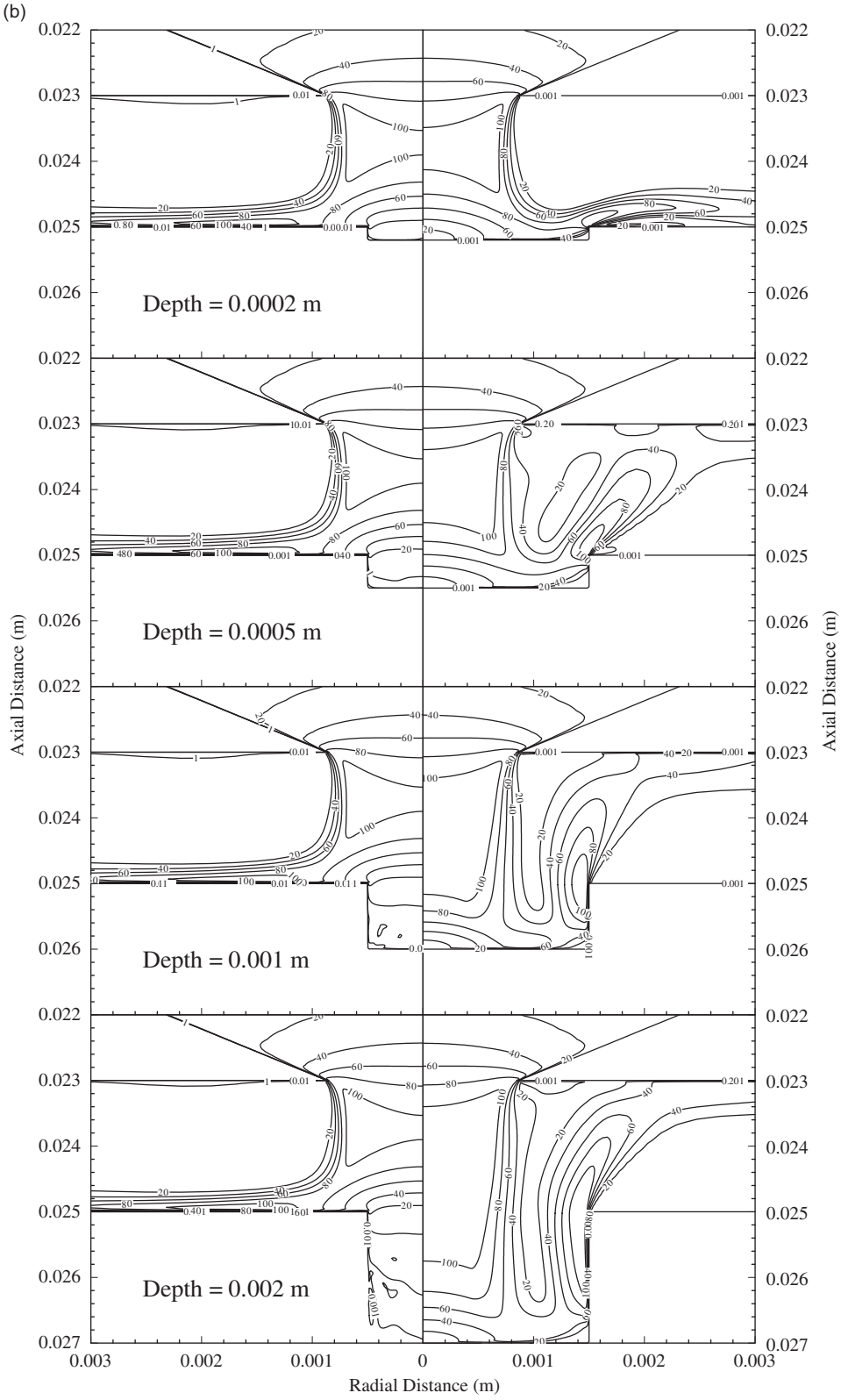

Fig. 3. (*Continued*)

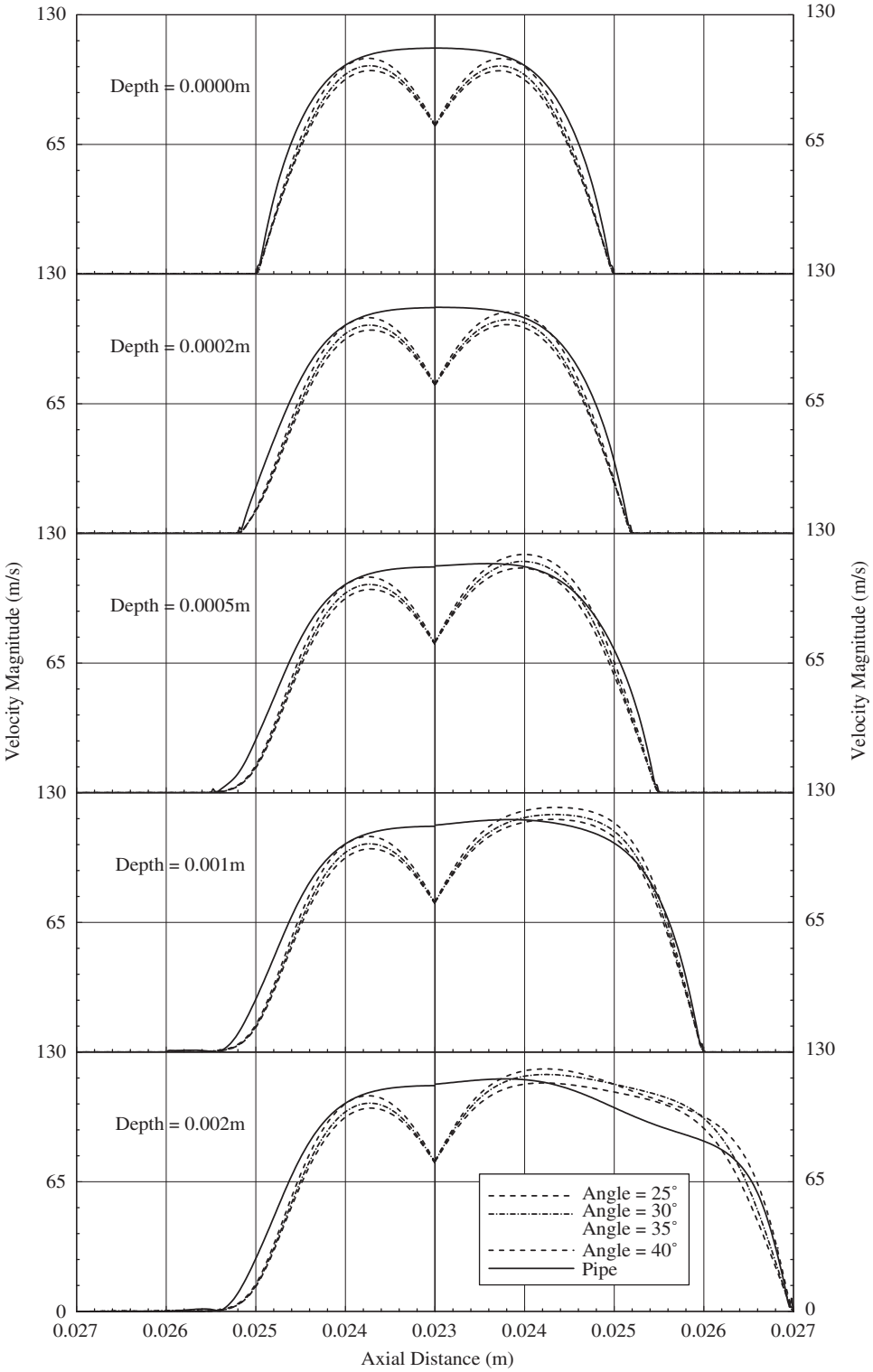

Fig. 4. Velocity magnitude along the symmetry axis for two different cavity diameters, four nozzle cone angles and pipe, and five depths.

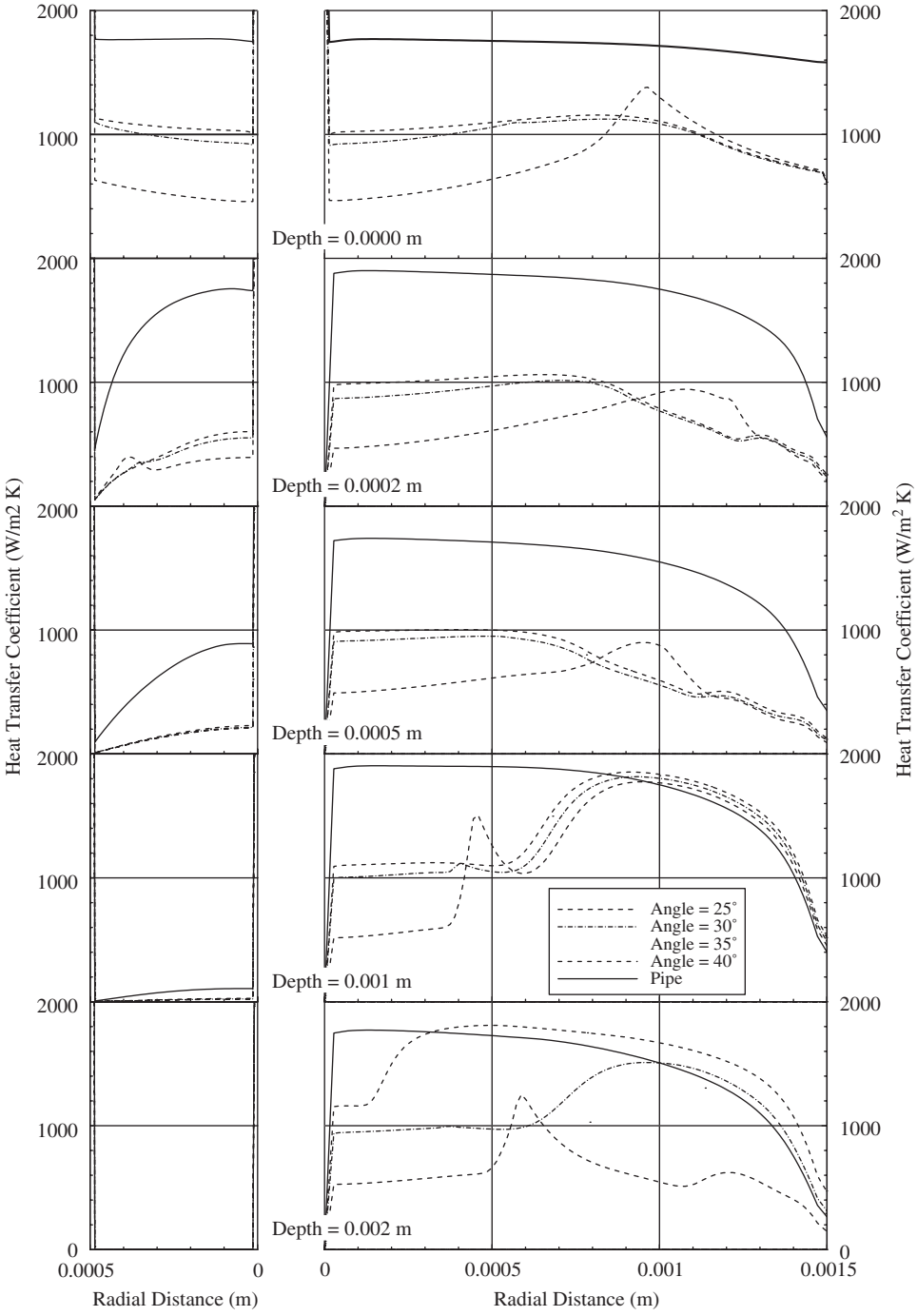

Fig. 5. Heat transfer coefficient at the cavity bottom in the radial direction for two different cavity diameters, four nozzle cone angles and pipe, and five depths.

Fig. 5 shows the heat transfer coefficient across the bottom of the cavity for two cavity diameters, four cavity depths, and four cone angles of the conical nozzle. The results obtained for the jet emerging from the pipe exit is also shown for comparison. The heat transfer coefficient varies significantly along the cavity bottom for different cone angles of the nozzle. Heat transfer coefficient curves do not follow a trend with increasing depth; however, it is enhanced towards the edge of the cavity when cavity depth increases. Heat transfer coefficients corresponding to a small cavity diameter

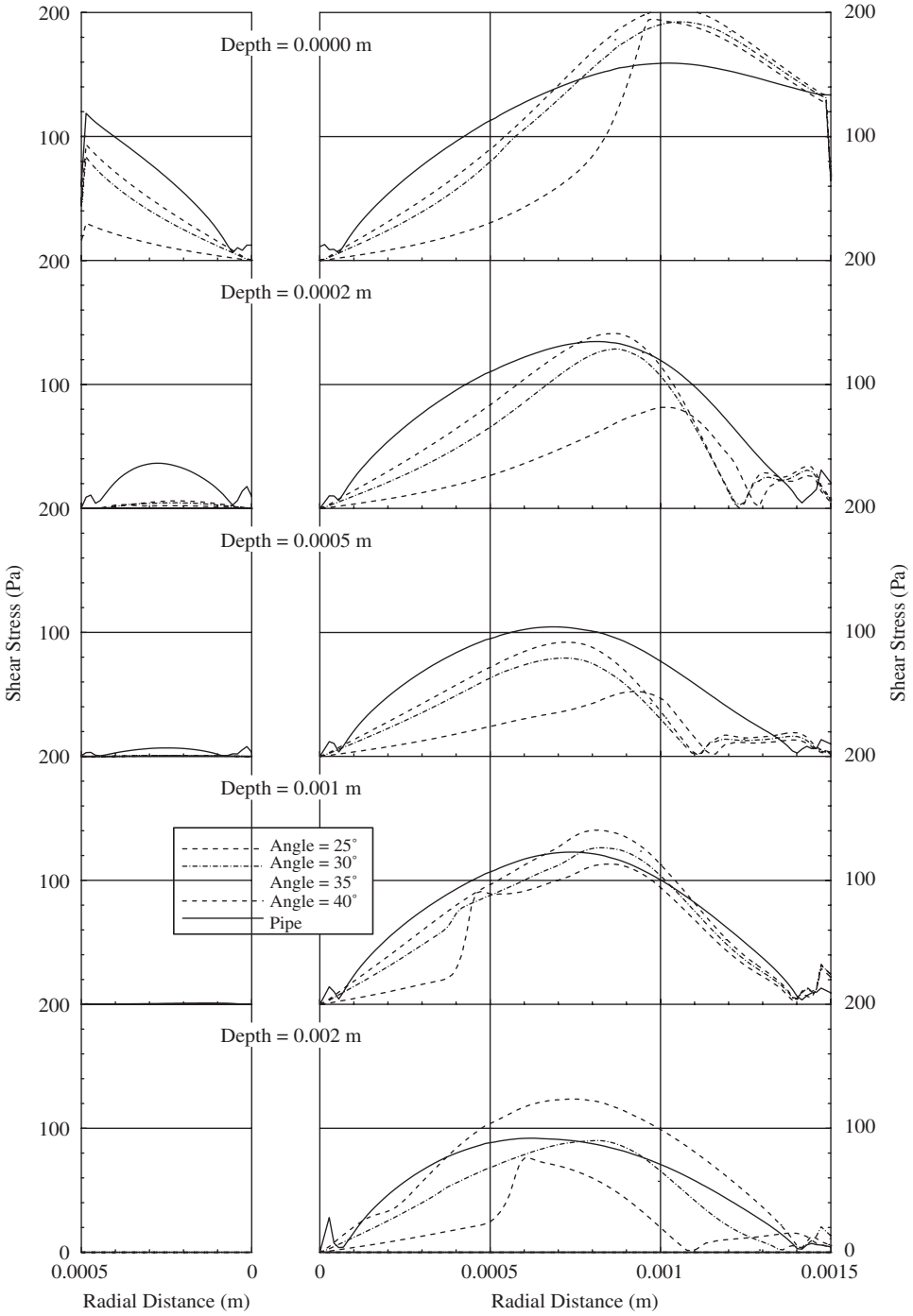

Fig. 6. Shear stress at the cavity bottom in the radial direction for two different cavity diameters, four nozzle cone angles and pipe, and five depths.

are smaller than that of the large diameter cavity. This is because of the flow structure formed in the cavity. The nozzle cone angle influences the heat transfer coefficient; in which case, a cone angle of 55° results in lower heat transfer coefficients as compared to its counterpart corresponding to other cone angles. The jet emerging from the pipe results in higher heat transfer coefficients than that corresponding to a nozzle for small cavity depths.

Fig. 6 shows the wall shear stress along the cavity bottom for two cavity diameters, four cavity depths and four cone angles of the conical nozzle. The wall shear stress is lower for the small cavity diameter than the large diameter. This is because of the flow field developed in the cavity, i.e. velocity magnitude is considerably smaller in the small diameter cavity. In the case of the large diameter cavity, wall shear stress reduces to almost zero in the region of the symmetry axis and the bottom edge of the cavity. This is because of the rate of fluid strain which reduces in this region. Moreover, due to the radial acceleration of the flow in the region close to the cavity bottom, the rate of fluid strain is enhanced mid-way between the symmetry axis and the cavity bottom edge. Consequently the shear stress attains high values in this region. The influence of nozzle cone angle on the shear stress is considerable as the depth of the cavity increases. In this case, the cone angle of 55° results in a low magnitude of shear stress at cavity bottom.

5. Conclusions

Jet impingement, emerging from a conical nozzle, onto a cylindrical cavity is considered in relation to laser gas-assisted operation. The influence of cone angle of the nozzle, cavity diameter and depth on flow structure in and around the cavity and heat transfer characteristics are examined. Air is used as the impinging gas, while stainless steel is considered as workpiece material. It is found that increasing cavity diameter modifies the flow structure in the cavity significantly. In this case, the velocity magnitude in the cavity increases and the stagnation region moves towards the cavity bottom surface. However, the stagnation zone moves slightly inside the cavity for a small diameter cavity. Therefore, flow in the cavity results in quite a small rate of fluid strain, i.e. the magnitude of shear stress becomes very small. Consequently, the frictional drag due to the impinging jet is minimal for the small diameter cavity, and the opposite is true for the large diameter cavity. The heat transfer coefficient is influenced by the cavity depth and diameter. Moreover, heat transfer coefficient curves do not follow a definite pattern; for deep cavities, the heat transfer coefficient increases towards the cavity edge. The influence of nozzle angle is important at low cone angles; in this case, a nozzle cone angle of 55° results in a low heat transfer coefficient and shear stress in the cavity.

Acknowledgement

The authors acknowledge the support of King Fahd University of Petroleum and Minerals, Dhahran, Saudi Arabia, through project SAB-2004/14 for this work.

References

Benocci, C., 1991. Introduction to the Modeling of Turbulence, 1991–02. Von Karman Institute for Fluid Dynamics.

Bizzak, D.J., Chyu, M.K., 1995. Use of a laser-induced fluorescence thermal imaging system for local jet impingement heat transfer measurement. International Journal of Heat and Mass Transfer 38 (2), 267–274.

Chen, S.L., 1998. The effects of gas composition on the CO_2 laser cutting of mild steel. Journal of Material Processing Technology 73, 147–159.

Elkaim, D., Reggio, M., Camarero, R., 1992. Simulating two-dimensional turbulent flow by using the $k-\varepsilon$ model and the vorticity-stream function formulation. International Journal for Numerical Methods in Fluids 14, 961–980.

Garimella, S.V., Rice, R.A., 1995. Confined and submerged liquid jet impingement heat transfer. ASME Journal of Heat Transfer 117, 871–877.

Hogg, S., Leschziner, M.A., 1989. Second-moment-closure calculation of strongly swirling confined flow with large density gradients. International Journal of Heat and Fluid Flow 10 (1), 16–27.

Hsu, M.J., Molian, P.A., 1995. Off-axial, gas-jet-assisted, laser cutting of 6.35-mm thick stainless steel. ASME Journal of Engineering for Industry 117, 272–276.

Huang, L., El-Genk, M.S., 1994. Heat transfer of an impinging jet on a flat surface. International Journal of Heat and Mass Transfer 37 (13), 1915–1923.

Kar, A., Rockstroh, T., Mazumder, J., 1992. Two-dimensional model for laser-induced material damage: effects of assist gas and multiple reflections inside the cavity. Journal of Applied Physics 71 (6), 2560–2569.

Launder, B.E., 1989. Second-moment closure and its use in modelling turbulent industrial flows. International Journal for Numerical Methods in Fluids 9, 963–985.

Man, H.C., Duan, J., Yue, T.M., 1997. Design and characteristic analysis of supersonic nozzles for high gas pressure laser cutting. Journal of Materials Processing Technology 63, 217–222.

Mohanty, A.K., Tawfek, A.A., 1993. Heat transfer due to a round jet impinging normal to a flat surface. International Journal of Heat and Mass Transfer 36 (6), 1639–1647.

Patankar, S.V., 1980. Numerical Heat Transfer. McGraw-Hill, New York.

Versteeg, H.K., Malalasekera, W., 1995. An Introduction to Computational Fluid Dynamics, The Finite Volume Method. Longman Scientific and Technical.

Yilbas, B.S., Sahin, A.Z., Davies, R., 1995. Laser heating mechanism including evaporation process initiating laser drilling. International Journal of Machine Tools and Manufacturing 35 (7), 1047–1062.

Yilbas, B.S., Shuja, S.Z., Budair, M.O., 2002. Stagnation point flow over a heated plate: consideration of gas jet velocity profiles. Arabian Journal of Science and Engineering 27 (2C), 91–116.

Yilbas, B.S., Shuja, S.Z., Budair, M.O., 2003. Jet impingement onto a hole with constant wall temperature. Numerical Heat Transfer, Part A 43 (8), 843–865.

Yilbas, B.S., Shuja, S.Z., Budair, M.O., 2004. Jet impingement onto a conical cavity with elevated wall temperature. International Journal of Numerical Methods for Heat and Fluid Flow 14 (8), 1011–1028.